CrossMark

RESEARCH PAPER

Thermal stability, phase transformation characteristics, and thermal properties of T91 steel and welding consumables

S. Raju[1] · Jeyaganesh B[2] · H. Tripathy[1] · S. Murugesan[1] · Saroja Saibaba[1] · S.K. Albert[1] · A.K. Bhaduri[1]

Abstract A comprehensive dynamic calorimetry and dilatometry characterization of thermal stability, thermal properties, and α-ferrite + carbides $\rightarrow$ γ-austenite phase transformation kinetics of T91 grade ferritic-martensitic (FM) steel, together with four of its SMAW consumables has been performed. In particular, the sequence of phase changes taking place right up to melting has been investigated. The on-heating α-ferrite $\rightarrow$ γ-austenite transformation temperatures, namely Ac_1, Ac_3, the dissolution temperatures of $M_{23}C_6$ and MX-type carbonitrides, and the solidus and liquidus temperatures are accurately measured along with associated enthalpies. The role of $(Ni + Mn)$ content in influencing the equilibrium solidification mode has been clearly delineated. It is found that both Ac_1 and Ac_3 temperatures vary in a nonlinear fashion with respect to the heating rate. Further, the Ac_1 temperature exhibits a pronounced decrease with increasing $(Ni + Mn)$ content. The kinetics of γ-austenite formation upon continuous heating has been modeled using a simple isochronal version of the Kolmogorov-Johnson-Mehl-Avrami (KJMA) formalism. A value of about 280 to 300 kJ mol^{-1} has been obtained for the effective activation energy (Q_{eff}) of the overall transformation. It is found that Q_{eff} is quite sensitive to the heating rate, and the observed transformation kinetics indicate that the presence of undissolved $M_{23}C_6$ and MX carbide particles plays an important role in the kinetics of reaustenitization reaction in high chromium steels. Finally, the specific heat C_p and the bulk thermal expansion ($\Delta l/l_o$) for both base metal for all four welding consumables have been determined.

Keywords (IIW Thesaurus) High alloy Cr Mo steels · Transformation · Solidification · Cooling rate · Thermal properties

1 Introduction

The design of materials, together with appropriate processing and fabrication into final engineering components is basically a complex decision-making process in the light of all available and critically assessed knowledge base on materials [1]. In the case of materials and process design for strategic applications, such as nuclear and advanced fossil power plants, it is often imperative to vet the choice of material composition and the associated fabrication process, against the stringent plant-safety auditing protocols as well. This latter requirement demands a high(er) degree of maturity and reliability on the part of design database(s) [1].

Welding constitutes a major joining process in the fabrication of power plant components [2]. The advent of newer grades of ferritic-martensitic (F-M) steels for nuclear applications [3–8] has catalyzed an extensive basic research program on welding metallurgy; especially, on those aspects that are related to tailoring the composition of welding consumables with a view to minimize, or avoid if possible, the formation of delta ferrite during the course of primary weld solidification [2, 9]. Thus, for an example, a fully primary austenitic mode of solidification may be ensured by carefully adjusting the combined concentration of γ-austenite stabilizing elements, such as Ni + Mn + Co + Cu + N + C etc., in welding consumables. In some high-temperature creep-resistant and radiation-induced

Recommended for publication by Commission IX - Behaviour of Metals Subjected to Welding

✉ A.K. Bhaduri
arunkbhaduri@gmail.com

[1] Metallurgy and Materials Group, Indira Gandhi Centre for Atomic Research, Kalpakkam 603102, India

[2] Formerly at Indira Gandhi Centre for Atomic Research, presently at Nuclear Advanced Manufacturing Research Centre, University of Sheffield, Rotherham S60 5WG, UK

Springer

swelling-tolerant F-M steels meant for fusion reactor applications, the partial replacement of Mo by W and or Ta; Nb by V etc., is widely practiced [4, 10–12]. In such cases, the presence of some amount of δ-ferrite phase is often found at the end of the primary solidification [13, 14]. On the other hand, while tailoring the composition range of austenite-stabilizing elements, one must also be aware of the resulting penalty in the form of low α-ferrite→γ-austenite transformation temperature, Ac_1. It is useful to reiterate that Ac_1 decides the upper limit for any postweld heat treatment (PWHT) of F-M steels [15, 16]. Thus, in nutshell, the appropriate balancing of the composition of welding consumable is important for proper tempering of martensite during PWHT, since the microstructure that results from an improper tempering at a temperature marginally higher than Ac_1 leads to reduced fracture toughness and embrittlement during service [17, 18]. On similar lines of reasoning, it may also be added that a comprehensive characterization of thermal stability and thermal properties is necessary for qualifying welding procedure specifications. It is in this perspective that an attempt has been made in the present study to gather these useful information on T91-grade ferritic-martensitic steel and four of its weld consumables, having different (Ni + Mn) content. The scope of this study is outlined below.

2 Scope of this study

The scope of this study includes the following:

1. Determination of the sequence of phase changes that occur during heating to and cooling from liquid
2. Determination of the heating rate sensitivity and the kinetics of α-ferrite + carbides→γ-austenite phase transformation
3. Determination of specific heat and thermal expansion characteristics
4. Elucidation of the role of (Ni + Mn) content in influencing phase stability

The principal experimental techniques adopted for this purpose are differential scanning calorimetry and dilatometry. These results are supplemented by optical metallography and microhardness investigations. However, before proceeding further, brief details about material and experimental procedures are provided in the following section.

3 Materials and experimental details

3.1 Composition and sample preparation

The T91 steel used in this study belongs to a commercial grade, whose composition as obtained by direct reading

optical emission spectrometry is specified in Table 1. The three weld consumables taken up for study are E 9016–B9 basic coated shielded metal arc welding (SMAW) electrodes obtained from three different commercial sources and are referred to herein as weld metal WM-A, WM-B, and WM-C, respectively. As can be seen from Table 1, these are characterized by progressively decreasing (Ni + Mn) content. The filler wire for gas tungsten arc welding (GTAW) has been obtained from another commercial source and is referred to as WM-D. A weld pad of dimension, $100 \times 75 \times 12$ mm is made by the SMAW process for the electrodes and by the GTAW method for the filler wire using the stringer bead technique. The diameter of SMAW electrode is 3.15 mm, while that of GTAW filler wire is about 1.6 mm. A total of eight layers were built without any interpass treatment. The following process parameters are adopted in making the weld pads: 90 A/25 V, heat input of 900–1000 J for SMAW of electrodes, and 80 A/15 V, heat input of 300 J for GTAW of WM-D. The samples for the present study were sliced from the portion that is located approximately 2 mm below the top surface of the weld pad. For optical metallographic characterization, the specimens were prepared in the standard manner, starting from coarse dry grinding to 1000 grade emery polishing and then to final finishing with alumina- and diamond-containing suspension. The polished samples were given a mild initial etching with a 2 % nital solution and then subsequently by the Villela's reagent for about a minute. These polished and etched samples were also used for room temperature X-ray diffraction (INEL®, Cu-K_α radiation, Ge-monochromator,

Table 1 Listing of compositional details (in weight percent) of T91 steel and the welding consumables (E9016-B9) used in this study (composition determined by direct reading optical emission spectroscopy)

Elements	WM-A	WM-B	WM-C	WM-D	T91 base metal
C	0.06	0.075	0.1	0.084	0.097
Mn	1.37	1.20	1	0.60	0.37
Si	0.30	0.30	0.24	0.30	0.31
Ni	0.95	0.65	0.7	0.75	0.38
P	0.005	0.008	0.009	0.007	0.018
S	0.001	0.007	0.012	0.0034	0. 0047
Cr	9.24	9.3	9.0	8.89	9.29
Mo	1.05	1.0	0.99	0.93	0.92
Nb	0.03		0.009	0.05	0.08
V	0.17	0.23	0.17	0.22	0.26
N	0.03	0.04	0.055	0.0375	0.057
Cu	–	–	<0.05	–	–
Al	–	–	<0.010	–	–
Fe	Balance	Balance	Balance	Balance	Balance
Mn + Ni	2.32	1.85	1.7	1.35	0.75
V + Nb	0.20	0.23	0.179	0.27	0.34

but with no source side filter) studies and microhardness (Leitz, 100 g) measurements. The X-ray results are processed by full profile refinement procedures using the proprietary software MAUD® (supplied by INEL®) to obtain the lattice parameter of the α-ferrite phase. As for microhardness data are concerned, eight measurements are made for on sample and the average value is reported in Table 2.

3.2 DSC experiments

The samples for differential scanning calorimetry (DSC) experiments were cut from thin sections sliced originally from the weld pad using diamond-coated wire saw. These were further cleaned and polished to regular and nearly identical cubes of mass varying from 50 to 70 ± 0.1 mg. The polishing of the sample disks is generally kept to a minimum extent to remove any macrosurface asperities, as otherwise the strain incurred during severe polishing may contribute to the baseline distortion of the DSC signal. The DSC experiments were performed with Setaram Setsys 16® heat-flux-type high-temperature differential scanning calorimeter, employing recrystallized alumina crucibles of about 100 μL volume. The crucibles were ultrasonically cleaned in methanol and rinsed with dilute HCl to remove any trace of contaminants arising from previous use. The full details of DSC equipment as well as the calibration procedure have already been discussed in our previous publications [19, 20]. Here, only the aspects that are relevant to this study are reiterated. Stated briefly, the experiments were performed under a constant flow (50 ml min^{-1}) of high purity argon (Iolar Grade I 99.993 % purity with moisture ≤2 ppm, nitrogen ≤2 ppm). A range of heating rates varying from 1 to of 100 K per minute is employed. Normally, it is found that lower heating rates (1–2 K min^{-1}) resulted in mild decarburization of the sample due to the appreciable resident time at high temperatures under argon gas cover, while high heating rates induce significant thermal lag between the actual sample temperature and that sensed by the noncontact thermocouple probe. Nevertheless,

the measurement of the mass before and after the experiment did not reveal any detectable change (≤0.01 g) even for samples that have experienced long residence times in our heat-flux DSC. As for the instrument-related thermal lag is concerned, a proper calibration of the heat-flux signal from sample is made using the reference output obtained on pure Fe (Aldrich, impurities ≤80 ppm of combined impurities). These calibration runs were made under identical experimental conditions (the sample mass and shape have been kept nearly the same for both reference and T91 samples). In the present study, it is estimated that for a heating rate of about 10 K min^{-1}, the thermal lag is about 5 K for T≤1200 K. For 1–3 K min^{-1} scan rate, it is about 3 K. For temperatures exceeding 1473 K, that is about $0.85T_m$ of the steel, the measured transformation temperatures are found to be accurate to ±15 K. Fresh samples were used for each DSC run, and multiple runs under identical conditions are performed for calibrating the precision of the transformation temperature. The temperature calibration is performed using recommended pure metal melting point standards, such as Sn, Al, Pb, In, and Au. The enthalpy calibration involves the accurate measurement of the peak area corresponding to the α-bcc→γ-fcc solid state transformation in case of pure iron [21]. The calibration constant (C) that is required for converting the peak area into specific enthalpy in J g^{-1} basis is obtained by making use of the critically assessed α-bcc→γ-fcc transformation enthalpy values [22]. The specific heat calibration is performed similarly using the literature data on the specific heat of pure iron [22]. It is observed that the measured solid-state transformation temperatures are accurate to ±5 K, while the liquidus temperatures are accurate to ±15 K. The transformation enthalpies are accurate to ±10 %. Since, reliable and reproducible temperature and heat flux calibration of DSC for cooling cycle is comparatively a difficult task; the enthalpy and the heat flow calibration of the signal were carried out only for the heating cycle in the present study. It is presumed that the accuracy of sample temperature measurement during cooling cycle is almost the same as that of the heating cycle [20].

3.3 DSC experimental schedule

The DSC experimental schedule consisted of heating the system from room temperature to an initial temperature of 473 K (200 °C) at the rate of 10 K min^{-1} and holding at this temperature for about 15 min. This is required for the attainment of thermal equilibrium of the system before starting any measurement. This is followed by the actual programmed heating, holding, and cooling schedules. In the present study, the sample is heated at a steady rate to 1773 K (1500 °C) followed by an isothermal hold of about 15 min at this temperature. Subsequently, the sample is cooled to 473 K (200 °C) at the preselected rate and is allowed a resident time of 15 min at this temperature, before it is finally cooled again to room

Table 2 Listing of Vickers microhardness values (VHN) for welding consumables and T91 base metal in normalized and tempered condition (italicized values are not considered in final analysis)

Sample no.	WM-A	WM-B	WM-C	WM-D	Base metal
1	473	503	503	560	339
2	493	483	514	572	336
3	488	498	514	560	339
4	488	503	514	542	322
5	488	483	514	548	342
6	488	464	514	519	351
Average	485	487	514	556	341

temperature. In the current investigation, we augmented this scheme by performing one more additional baseline run at the end of the abovementioned three-run schedule. This was done in order to ensure or assess the extent of the baseline reproducibility at the end of each experimental schedule. A good agreement between the start and finish baselines is suggestive of the stable thermal dynamics of the entire DSC module and the temperature sensor. Besides, it also implies that the sample side crucible remains fairly uncontaminated during the entire course of experiment. The heating and cooling rates were varied from 1 to 99 K min^{-1}.

3.4 Dilatometry measurements

The primary purpose of carrying out dilatometry is to obtain bulk thermal expansion ($\Delta l_T/l_o$) estimates, although it is instructive to note that transformation kinetics of $\alpha \rightarrow \gamma$ and $\gamma \rightarrow \alpha'$-martensite phase changes can also be studied by dilatometry [23]. However, it must be added that the relative accuracy of measured transformation temperatures is better in a controlled DSC experiment than in bulk dilatometry, where temperature gradient across the sample length is unavoidable. In the present study, $\Delta l_T/l_o$ measurements have been performed with Setaram Setsys evolution TMA 16 equipment which is a vertically mounted single pushrod-type dilatometer equipped with a resistance-heated graphite furnace and an LVDT sensor for measuring the temperature-induced linear dimensional strain ($\Delta l_T/l_o$). Samples for high-temperature dilatometry are taken in the form of small rectangular (20×20 mm) slices, which are polished to mirror finish using standard metallographic procedures to yield smooth and flat surface. The starting thickness of the sample has been measured by a digital vernier gauge to better than ± 0.01 mm. Pure α-alumina disks with known bulk thermal expansion values are used as calibration standard [23]. Two different heating/cooling rates, namely 10 and 7 K min^{-1} were employed in the present study, and the 7 K min^{-1} data are used for estimating thermal expansion data. The entire experiment has been carried out in flowing high purity argon gas atmosphere. In our recent study on 9 % Cr-based reduced activation F-M steel, the calibration of temperature and bulk dilatational strain (Δl) in dilatometry measurements have been carried out using pure iron as the standard (Sigma-Aldrich iron with 80 mass ppm of combined impurities), and this calibration is maintained in the present study as well. The relative accuracy of the normalized dilatational strain ($\Delta l/l_{300}$) has been estimated to be ± 5 %. Using the known value for the α-bcc $\rightarrow \gamma$-fcc on-heating transformation temperature of iron, it is estimated that measured transformation temperatures are accurate to ± 10 K. The transformation temperature has been determined by the method of intersection of leading tangents to the dilatometry trace at the transformation start and finish temperatures.

4 Results

4.1 Optical metallography and microhardness measurements

In Fig. 1a, d, the typical optical micrographs of the four weld metals WM-A to WM-D are presented. Figure 1e portrays the microstructure of tempered T91 base metal. In the case of weld metals, the characteristic martensite microstructure is clearly observed. It may be added that although no interpass heat treatment was attempted while building up the weld bead, the samples having been sliced at approximately 2 mm below the top surface, have suffered some tempering due to the heat effects generated during the last welding pass. Thus, the microstructure of WM-A (Fig. 1a) reveals a finer acicular martensite with no clear trace of prior austenite boundaries. In the case of WM-B (Fig.1b), the presence of a nicely outlined prior austenite grain structure within, which some sporadic coarse carbide particles are dispersed, is readily apparent. The microstructure of WM-C (Fig. 1c) reveals a coarser and somewhat patchy martensite formation, while that of WM-D (Fig.1d) indicates considerable coarsening. Figure 1e on the other hand is typical of tempered martensite microstructure with an extensive decoration of the ferrite subboundaries by carbide particles.

It should be mentioned that this varying spectrum of microstructure witnessed at the level of optical microscopy is due to the different extent of residence time that each weld metal composition spends in different phase fields during its thermal history. In Table 2, the microhardness values measured on each sample, under a load of 100 g, are tabulated.

4.2 X-ray diffraction

In Fig. 2, the room temperature X-ray diffraction profiles obtained on different samples using Cu-K$_\alpha$ radiation are collated together. The dominant peaks of bcc α-ferrite phase are clearly marked. In addition, few very weak peaks arising from (Fe, Cr)$_{23}$C$_6$ carbide are also observed [24]. The lattice parameter for the α-ferrite phase in T91 base metal is estimated to be 0.2873 ± 0.003 nm. It may be noted that this value is nearly the same for all the samples investigated here. The average of α-ferrite lattice parameter value is in good agreement with reported data on related 9 % Cr-based steels [21, 23].

4.3 DSC results on transformation temperatures and transformation enthalpy

In Fig. 3a, a typical slow-scan (1 K min^{-1}) DSC profile obtained on the sample WM-C is illustrated. In Fig. 3b, an expanded view around the melting region is portrayed for all the four welding consumables. In order to avoid multiplicity of figures, the full profile for only one consumable is shown in Fig. 3a. The data on others are presented in Table 3. At the outset, it

Fig. 1 Optical micrographs of **a**–**d**different weld consumables: **a** WM-A, **b** WM-B, **c** WM-C, **d** WM-D, and **e** tempered T91 base metal
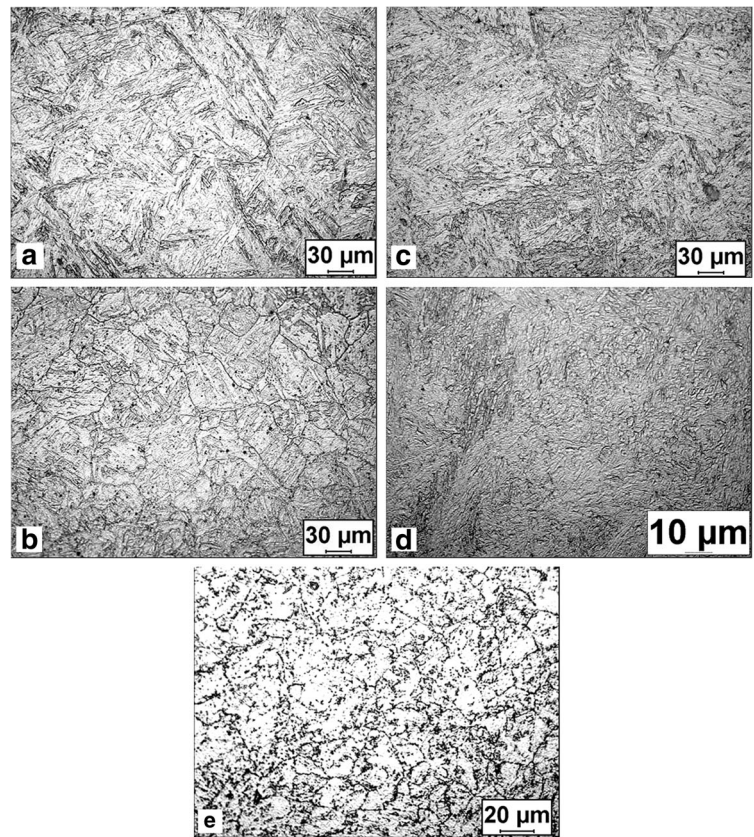
must be mentioned that transformation temperature data on T91 base metal has already been presented in one of our earlier published work [21]; however, these data are recalled here with a view to facilitate the easy comparison of thermal stability of different T91 weld consumables, as against the base metal. Nevertheless, the qualitative features of the DSC profiles are much the same for all compositions, with only the onset and finish temperatures of various phase transformations being
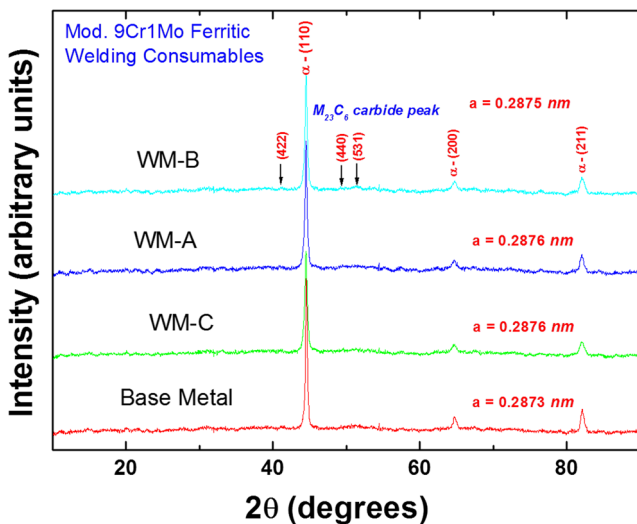

Fig. 2 Room temperature X-ray diffraction profiles of different welding consumables and T91 base metal taken using Cu-K$_\alpha$ radiation
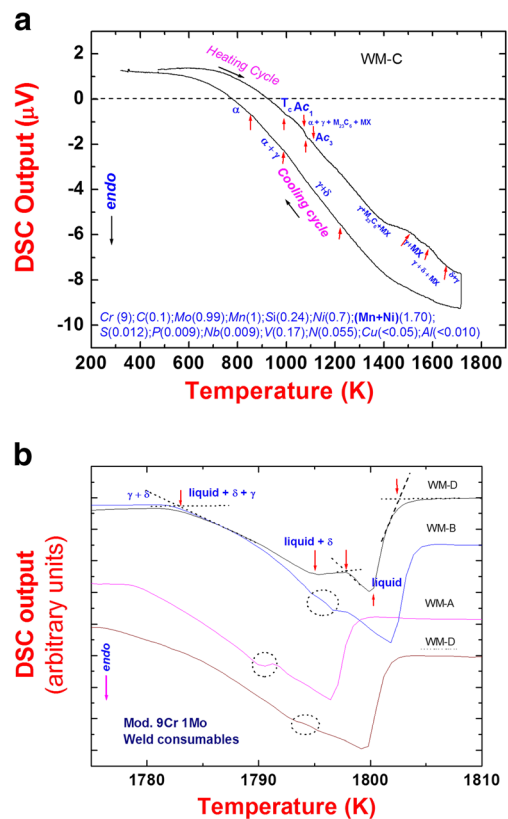

Fig. 3 **a** Slow-scan heating/cooling cycle DSC profile for WM-C sample; **b** expanded view around melting for all four weld consumables

Table 3 The on-heating phase transformation temperatures for various T91 consumables measured in this study are compared with similar data on T91 steel obtained from Jeyaganesh et al. [21]

Description of phase change	Transformation temperature, K (°C)				
	WM-A	WM-B	WM-C	WM-D	T91 base metal
α'-Martensite $\rightarrow \alpha$-ferrite + $M_{23}C_6$	947 (674)	937 (664)	930 (657)	944 (671)	903 (630)
T_c, Curie temperature	1003 (730)	1013 (740)	1004 (731)	1004 (731)	1012 (739)
α + (V,Nb)(C,N) + $M_{23}C_6 \rightarrow \alpha + \gamma$ + (V,Nb)(C,N) + $M_{23}C_6$ (Ac_1)	1045 (772)	1080 (807)	1072 (799)	1072 (799)	1102 (829)
$\alpha + \gamma$ + (V,Nb)(C,N) + $M_{23}C_6 \rightarrow \gamma$ + (V,Nb)(C,N) + $M_{23}C_6$ (Ac_3)	1100 (827)	1117 (844)	1120 (847)	1120 (847)	1138 (865)
γ + (V,Nb)(C,N) + $M_{23}C_6 \rightarrow \gamma$ + (V,Nb)(C,N)dissolution of $M_{23}C_6$	1522 (1249)	1520 (1247)	1513 (1240)	1543 (1270)	1522 (1249)
γ + (V,Nb)(C,N) $\rightarrow \delta + \gamma$ + (V,Nb)(C,N)	1583 (1310)	1572 (1299)	1567 (1294)	1598 (1325)	1573 (1300)
$\delta + \gamma$ + (V,Nb)(C,N) $\rightarrow \delta + \gamma$ dissolution of (V,Nb)CN	1653 (1380)	1599 (1326)	1632 (1359)	1655 (1382)	1659 (1386)
$\delta + \gamma \rightarrow$ liquid + $\gamma + \delta$ (solidus)	1790 (1517)	1795 (1522)	1793 (1520)	1795 (1522)	1793 (1520)
Liquid + $\gamma + \delta \rightarrow$ liquid + δ	1793 (1520)	1796 (1523)	1796 (1523)	1798 (1525)	1794 (1521)
Liquid + $\delta \rightarrow$ liquid (liquidus)	1800 (1527)	1806 (1533)	1804 (1531)	1806 (1533)	1802 (1529)
$\Delta^o H_f$, Enthalpy of melting (J g^{-1})	240	266	242	241	239
$\Delta^o H_{\alpha \rightarrow \gamma}$, Enthalpy of $\alpha \rightarrow \gamma$ transformation (J g^{-1})	8	26	17	16	13

Source: Jeyaganesh et al. [21]. Values quoted in brackets are in °C

different for different composition. A careful inspection of Fig. 3a, b suggest, in the light of available literature information on high Cr steels, the following sequence of phase transformations with increasing temperature [13, 25–27].

1. Ferromagnetic to paramagnetic transformation occurs at T_c, the Curie point of the α-ferrite phase. Depending on composition, T_c is found to vary from 730 to 740 °C.
2. The α-ferrite + $M_{23}C_6$ + MX $\rightarrow \gamma$-austenite + $M_{23}C_6$ + MX, diffusional phase transformation occurs upon on crossing the Ac_1 temperature. Depending on the heating rate, the transformation reaches a fair degree of completion at Ac_3. It has been generally observed in case of high chromium steels that dissolution of $M_{23}C_6$ phase is realized only to a small extent during the reaustenitization step [28–30], although the Thermo Calc® based equilibrium simulations on 9 % Cr and specifically the Ta/W added variety, suggest some finite dissolution (~5 %) by the time Ac_3 is reached on very slow heating [13, 26, 27].
3. Next, in the γ-austenite phase, the dissolution of $M_{23}C_6$ occurs through the diffusional reaction, $\gamma + M_{23}C_6$ + MX $\rightarrow \gamma$ + MX. Basically, the dissolution of $M_{23}C_6$ carbide in γ-austenite is a continuous reaction taking place during isochronal heating. After crossing the Ac_3 temperature, it is generally seen as a shallow endothermic trough in an otherwise smooth DSC profile [13]. This dissolution thermal arrest is observed better in slow heating rate scans. The following transformations take place after the dissolution of $M_{23}C_6$ carbide in γ-austenite.
4. γ + MX $\rightarrow \delta$-ferrite + γ + MX (appearance of high temperature δ-bcc ferrite phase).
5. $\delta + \gamma$ + MX $\rightarrow \delta + \gamma$ (dissolution of MX phase in γ-austenite).
6. $\delta + \gamma \rightarrow$ Liquid + $\delta + \gamma$ (first appearance of liquid).
7. Liquid + $\delta + \gamma \rightarrow$ Liquid + δ (dissolution of γ in liquid).
8. Liquid + $\delta \rightarrow$ Liquid (completion of melting).

The region covered by the last three thermal arrests constitutes the solidus–liquidus temperature interval (see Table 3). In the case of 9–12 % Cr ferritic-martensitic steels having a host of other elements like Mo, W, Ta, Nb, V, Mn, Ni, Co, N, B, etc., with a nominal carbon concentration of about 0.1 wt.%, the observed solidification characteristics are not only a function of composition, that is effective $[Cr]_{eq}/[Ni]_{eq}$ ratio, but also of the cooling rate from liquid.

Thus, there could be significant differences between the experimentally observed phase formation sequence and that predicted by equilibrium ThermoCalc® software simulations [13, 20]. This difference is mostly kinetic in origin [13]. Thus, for an example, the equilibrium phase equilibrium simulation for a typical T91 composition may suggest only a small existence domain for the liquid + $\delta + \gamma$ three-phase coexistence under normal slow cooling conditions [25–27]. The real-time solidification scenario is, however, dependent on kinetic factors which are influenced by composition, cooling rate, and most importantly, the solidification or weld geometry which influences the temperature gradient ahead of the liquid/solid interface. After the primary formation of δ-ferrite from liquid (L $\rightarrow \delta$) is realized, it is very likely that the remaining interdendritic liquid will be rich in Ni and Mn (also Co, if present), since these elements tend to partition only a little toward δ-bcc ferrite. If in addition, the undercooling of

remaining interdendritic liquid is adequate enough to nucleate γ-austenite, then the remaining liquid would solidify as, $L \rightarrow \delta \rightarrow L + \delta + \gamma$. It is clear therefore that such possibility is dependent both on the concentration of bcc-stabilizing elements and cooling rate. Under high cooling rates, the extent of partitioning of Nb, Ta, W, Si, etc., to δ-ferrite would be much less, resulting indirectly in low supersaturation of the interdendritic liquid with respect to austenite-stabilizing elements. Further, it is also possible that a high cooling rate would facilitate a deeper undercooling of liquid, which under favorable circumstances, can help in nucleating γ-austenite in a massive manner. This possibility has been experimentally established in the case of directional solidification of austenitic stainless steels [31, 32]. However, high chromium ferritic-martensitic steels still await a detailed investigation in this respect. Nevertheless, in general terms, it may be said that in F-M steels, the secondary $L \rightarrow \gamma$-austenite formation takes place, in order to relieve the high local supersaturation of liquid with respect to Ni + Mn. In this manner, both composition and cooling rate mediated kinetic effects dictate the solidification path of ferritic-martensitic steels in a combined manner.

As may be seen from Fig. 3b, the presence of a higher austenite-stabilizing (Ni + Mn) content in the welding consumables as against the base metal composition (Table 1) supports that liquid + δ + γ coexistence is in principle possible during slow (1 K min^{-1}) solidification experiments. In Fig. 3b, it is also interesting to note the subtle difference in the nature of DSC profiles obtained for different weld consumables around liquid + δ-ferrite region. A somewhat flat or horizontal portion, such as the one witnessed for WM-D (Fig. 3b, enclosed in dotted circle), suggests that solidification occurs for this composition in a peritectic-like manner; that is, $L \rightarrow L + \delta$ reaction takes place over a narrow range of temperature with no continuous heat effect, as compared to other compositions. But, an unambiguous experimental verification of this possibility needs further critical scrutiny.

In the case of T91 base metal, the $M_{23}C_6$ and MX phases refer, respectively, to $(Cr,Fe)_{23}C_6$ and $(V,Nb)(C,N)$ type mixed carbides and carbonitrides [13, 26]. It must also be mentioned that for a given DSC instrument and for set of prescribed experimental conditions, the sharpness of various transformation peaks is a function of enthalpy effect. Unlike the case of $\alpha \rightarrow \gamma$ structural transformation or $\delta \rightarrow L$ melting reaction in pure Fe, the solid-state phase changes taking place in steel, like the dissolution of $M_{23}C_6$ and MX carbide phases are accompanied by only a small change in enthalpy [13]. Therefore, these changes manifest as mild, yet distinct inflections in the baseline compensated DSC profile. The enthalpy effects associated with $\alpha \rightarrow \gamma$ phase change, and melting are given directly in terms of the total area enclosed under respective peak. The conversion factor required for getting enthalpy in terms of J g^{-1} is obtained from the corresponding signal from pure iron [21, 22]. The enthalpy values estimated in this manner are listed in the last two rows of Table 3.

As for α-ferrite + carbides $\rightarrow$ γ-austenite phase change is concerned, there is reasonable agreement among the transformation enthalpy values recorded for WM-C, WM-D, and base metal. But, the corresponding values for both WM-A and WM-B are off from this general trend. At this juncture, it must be mentioned that for heating rates in the range 1–10 K min^{-1}, the nature of $\alpha \rightarrow \gamma$ transformation peak for WM-A is found to be diffuse, contributing thereby to a higher degree of uncertainty in the measured peak area and hence in enthalpy values. In addition, an inspection of the composition of WM-A suggests a relatively higher Ni + Mn content, which means the measured enthalpy corresponds almost exclusively to the conversion of relatively more destabilized α-ferrite into γ-austenite. In addition, the low carbon concentration of about 0.06 wt.% of WM-A supports the argument that it is mostly the substitutionally alloyed α-ferrite matrix that is getting transformed to austenite in the Ac_1–Ac_3 intercritical domain; any probable contribution from possible $M_{23}C_6$ dissolution is expected to be minimal in this case. Both these factors serve to decrease the enthalpy of α-ferrite + carbide $\rightarrow$ γ-austenite phase change. The measured melting enthalpy values are in the range 240–260 J g^{-1}. These values are in line with typical values observed for high chromium–low carbon ferritic-martensitic steels [13, 21, 33].

4.4 Kinetics of α-ferrite + carbides $\rightarrow$ γ-austenite transformation

Since α-ferrite + carbides $\rightarrow$ γ-austenite phase transformation is a nucleation and growth controlled process, the observed transformation onset Ac_1 and finish Ac_3 temperatures show appreciable dependence on the rate of heating, β (Table 4). This aspect is graphically illustrated in Fig. 4a, b for the weld consumable WM-C. For other consumables, the relevant data are listed in Table 4. In Fig. 4a, the change in the sharpness of the α-ferrite + carbides $\rightarrow$ γ-austenite peak profile with increasing heating rate is depicted. The methodology adopted for obtaining Ac_1 and Ac_3 is also marked in this figure. In Fig. 4b, the heating rate dependencies of Ac_1, Ac_3, and $\alpha \rightarrow \gamma$ peak temperatures are brought out. It is clear that the transformation characteristics are strongly nonlinear with respect to heating rate, β especially, in the range 1–40 K min^{-1}. The measured variation of the transformation temperatures with β can be satisfactorily expressed by the following power law representation.

$$T_f(\beta) \; = \; T_o(\beta/\beta_o)^m \tag{1}$$

In Eq. (1), $T_f(\beta)$ stands for the general transformation temperature T_f, measured as a function of heating rate β,

Table 4 Listing of measured α-ferrite $+ M_{23}C_6 \rightarrow \gamma$-austenite phase transformation temperatures (Ac$_1$, Ac$_3$, and peak) for four modified 9Cr-1Mo welding consumables as a function of heating rate

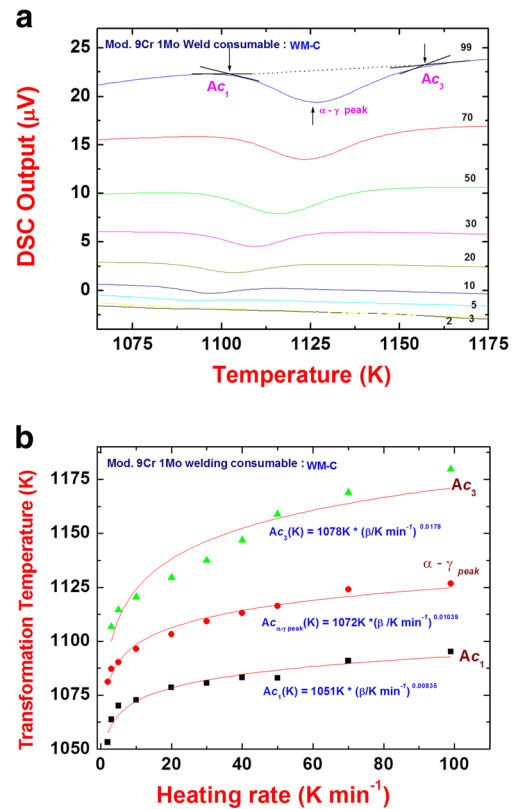| Heating rate (K min^{-1})	Ac$_1$ (K)	Peak (K)	Ac$_3$ (K)	Ac$_3$-Ac$_1$ (K)
WM-C				
2	1053	1081	1117	64
5	1064	1087	1107	43
10	1070	1090	1115	44
20	1073	1097	1120	48
30	1079	1103	1130	51
40	1081	1109	1137	57
50	1083	1113	1147	64
60	1083	1116	1159	76
75	1091	1124	1169	78
100	1095	1126	1180	85
WM-B				
3	1072	1087	1112	40
5	1075	1094	1111	36
10	1080	1099	1117	37
20	1081	1107	1127	45
30	1085	1110	1136	51
40	1088	1113	1143	55
50	1091	1118	1153	62
60	1093	1118	1153	60
75	1095	1121	1162	68
100	1103	1131	1177	73
WM-A				
5	1028	1064	1099	71
10	1045	1077	1101	56
20	1049	1085	1118	69
30	1048	1085	1122	74
40	1052	1093	1138	86
50	1056	1093	1147	91
60	1062	1099	1148	86
75	1071	1113	1154	83
100	1084	1111	1159	75
WM-D				
3	1094	1108	1125	30
5	1098	1111	1129	31
10	1104	1116	1137	33
20	1105	1121	1145	40
30	1108.	1125	1155	47
40	1109	1129	1165	56
50	1109	1133	1174	65
60	1111	1136	1178	67
75	1116	1140	1189	73
100	1119	1144	1198	79

Fig. 4 Variation of **a** α-ferrite + carbides $\rightarrow$ γ-austenite transformation peak profiles; **b** transformation temperatures Ac$_1$, Ac$_3$, and α-ferrite $\rightarrow$ γ-austenite peak with heating rate

unity ($\beta_o = 1$). In such a case, T_o becomes equal to the observed transformation temperature at unit heating rate. From Fig. 4b, it is evident that Ac$_3$ is more sensitive to the heating rate variation than Ac$_1$. This important fact contributes to the kinetics-induced widening of the ($\alpha +$ γ) two-phase field, namely the intercritical region for higher heating rates. This is also inferred from the increasing values of (Ac$_3$-Ac$_1$) with β (Table 4). The possible reason for this behavior is the fact that α-ferrite + carbides $\rightarrow$ γ-austenite transformation gets progressively more difficult during its final stages, possibly due to the reduction in driving force [27] and also due to hard impingement effects which contribute to incomplete finishing of the transformation at Ac$_3$ [29, 33–37]. Although the latter aspect is true for slow heating rate as well, the steeply rising nature of Ac$_3$ is markedly evident for higher β values [37].

The fraction of austenite f(T) formed as a function of temperature in the intercritical zone (Ac$_1 \leq T \leq$ Ac$_3$) is estimated using the following expression [38].

T_o is the transformation temperature for an arbitrarily chosen reference heating rate (β_o), and m is the power law exponent. For convenience, β_o may be taken as

$$f(T) = \left\{ \left({}_{Ac1}\!\int^{T} \varphi \, dT \right) \Big/ \left({}_{Ac1}\!\int^{Ac3} \varphi \, dT \right) \right\} \quad (2)$$

Here, $_{Ac1}\int^T \varphi\ dT$ is the partial area under the peak in the temperature domain Ac_1–T. The denominator $_{Ac1}\int^{Ac3} \varphi\ dT$ stands for the total peak area covering the entire transformation temperature range. The transformation plots obtained using Eq. (2) are displayed in Fig. 5 for the weld consumable WM-C. In deference to brevity, the data for other materials are not presented in graphical form. It is clear from Fig. 5 that austenite formation supports the classical sigmoid behavior, which is characteristic of a nucleation and growth phenomenon. In the usual methodology adopted for analyzing the transformation kinetics on continuous heating, the following functional form is often invoked to represent the instantaneous reaction rate, $(\partial f/\partial T)_\beta$ [38–41].

$$(\partial f/\partial T)_\beta = f(\gamma)k(T)(1/\beta) \qquad (3)$$

In this formalism, $f(\gamma)$ is a function of fraction austenite formed, often taken to be an empirical, but suitable reaction model that is consistent with the established kinetic features of the transformation under consideration. The empirical rate constant $k(T)$ is normally assumed to follow the Arrhenius form.

$$k = k_0 \exp\left(-Q_{eff}/RT\right) \qquad (4)$$

Here, Q_{eff} is the effective or apparent activation energy for the overall transformation process. In any formal theoretical development of the overall transformation kinetics for a nucleation and growth process, Q_{eff} is identified with a suitable physically based model of nucleation and growth [34, 38–40]. In such a case, it can be shown that Q_{eff} is a weighted sum of individual activation energies involved in nucleation and growth processes [38, 40, 42]. For the case of α-ferrite + carbides → γ-austenite transformation, the activation energy for nucleating γ-austenite phase, namely Q_N, is assumed to be smaller than that involved in propagating the γ/α transformation interface into transforming α-ferrite Q_G [35, 36]. In deference to the broad-based scope of this study, the theoretical treatment of the

transformation kinetics will not be attempted here; nevertheless, it is sufficient to note that relative values of Q_{eff} can be given a consistent physical interpretation.

In the present study, the overall transformation kinetics is fitted to the following nonisothermal version of the Kolmogorov-Johnson-Mehl-Avrami (KJMA) model for the fraction of austenite f(T) formed as a function of temperature at a constant heating rate [42].

$$f(T) = 1-\exp\left\{-k^n\left[R(T-T_S)^2/\beta\,Q_{eff}\right]^n\right\} \qquad (5)$$

It may be noted that in the above model, we have chosen $T-T_S$, the temperature increment with respect to the experimentally observed onset temperature (T_S) as the independent variable, since this corrects, in an apparent manner, for the error incurred in not accounting precisely for the true start of the transformation corresponding to zero transformed fraction, that is $f = 0$. The experimental data on f(T) for different heating rates (β) are fitted using Eq. (5) by means of a standard nonlinear optimization routine and the resulting values for the kinetic quantities namely Q_{eff}, k_0, and n are listed in Table 5. It is interesting to note that notwithstanding the difference in composition, there is a good agreement seen among the Q_{eff} values obtained for different weld consumables. The average value of n, the Avrami exponent for the overall transformation kinetics, is about 1. It also emerges from Table 5, that the kinetic parameters are sensitive to the heating rate; in particular, the apparent activation energy Q_{eff} exhibits a mild decrease with increasing heating rate (β). This point will be addressed in the "Discussion" section.

4.5 Specific heat measurements

One of the objectives of this study is to generate specific heat data for the weld consumables used in this study. It is hoped that such data are useful in thermal modeling of various physicochemical phenomenon taking place during welding. Although it is argued in literature that heat capacity values obtained by dynamic calorimetry are somewhat inferior to values measured by equilibrium adiabatic (static) calorimetry, we have earlier adopted DSC for obtaining fairly consistent estimates of C_p for 9 % Cr-based ferritic-martensitic steel having W and Ta [43]. In the present study, we have adopted the similar practice and used 5 K min^{-1} as the heating rate, with samples of slightly larger mass (~175 mg) to get appreciable signal. α-Alumina supplied by Setaram, has been used as primary standard, using which the C_p of pure Fe with 40 mass ppm of impurity has been characterized. This is then used as the secondary standard to estimate the C_p of 9 % Cr-based weld consumables. The method of ratios has been used to estimate C_p by DSC [43]. In this method, Cp is given by the following formula [43].

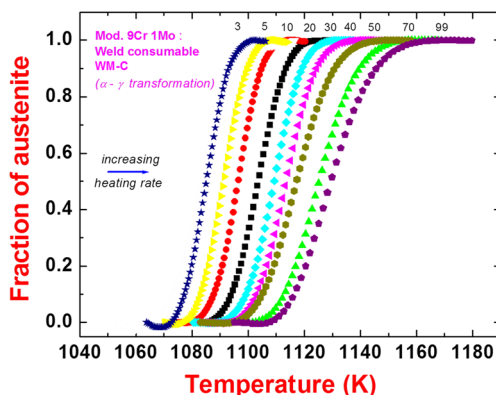$$C_P^S = C_P^R \times (m_R/m_S) \times \{(\mu_S-\mu_b)/(\mu_R-\mu_b)\} \qquad (6)$$

Fig. 5 Fraction of austenite formed as a function of temperature for different heating rates

Table 5 Listing of KJMA model fit parameters for α-ferrite + $M_{23}C_6 \rightarrow \gamma$-austenite phase change upon continuous heating

Heating rate (K min^{-1})	Q_{eff} (kJ mol^{-1})	k_0 (10^{15} s^{-1})	n	Heating rate (K min^{-1})	Q_{eff} (kJ mol^{-1})	k_0 (10^{14} s^{-1})	n
WM-C				WM-A			
2	313	1.27	1.26	3			
5	308	3.02	1.38	5	297	6.67	0.70
10	298	1.32	1.50	10	296	1.31	0.91
20	296	1.47	1.37	20	295	8.83	1.18
30	294	1.15	1.49	30	292	9.77	1.14
40	291	0.81	1.45	40	290	6.77	0.99
50	288	0.53	1.31	50	287	6.15	1.13
70	284	0.41	1.28	75	282	2.17	1.08
99	281	0.34	1.17	99	281	5.58	0.93
WM-B				WM-D			
3	291	0.43	1.26	3	320	92.86	0.90
5	289	0.44	1.44	5	312	79.64	1.14
10	286	0.55	1.45	10	305	37.31	1.13
20	283	0.38	1.60	20	302	25.81	1.17
30	283	0.45	1.52	30	299	23.83	1.16
40	280	0.38	1.41	40	295	18.23	1.17
50	279	0.28	1.35	50	292	17.5	1.09
60	276	0.31	1.28	60	288	10.64	1.18
99	273	0.17	1.22	99	286	1.085	1.01

In Eq. (6), C_P^S and C_P^R stand for the specific heat of sample and the reference. m_S and m_R denote respectively the masses of sample and reference. μ_S is the DSC signal in microvolt obtained with the sample, while μ_R is the corresponding quantity obtained with the reference material. The quantity μ_b is the baseline signal obtained with empty alumina crucibles. In Fig. 6, the measured C_p is plotted against temperature for modified 9 % Cr-based metal. It may be added that C_p versus T data measured for weld consumables are qualitatively similar, differing slightly in the magnitude of peak C_p at T_c, the Curie temperature, and also in the peak C_p values recorded at α-ferrite + carbide $\rightarrow \gamma$-austenite transformation region.

In view of the phase transformations encountered during heating, namely, (i) $\alpha_{ferro} \rightarrow \alpha_{para}$ and (ii) α-ferrite + carbides $\rightarrow \gamma$-austenite, it is not possible to fit the measured C_p versus T data by a single expression for the entire temperature range. Instead, a piecewise continuous description is attempted in this study. The measured C_p-T data are fitted to the following empirical form, suggested earlier by Kempen et al. [44], for pure iron.

$$C_P(T)/J\ kg^{-1}\ K^{-1} = A + BT + CT^2 + DT^{-2}$$
$$+ E\ exp(FT^*)(T^*)^G \qquad (7)$$

where

$$T^* = (T - T_R)/|T_R| \qquad (8)$$

$T_R = T_c$, in the temperature interval 473 K $\leq$ T $\leq T_C$ characterizing the ferromagnetic α-ferrite regime. For temperatures higher than T_c but less than Ac_1, that is $T_C \leq T \leq Ac_1$, characterizing paramagnetic ferrite region, another fit is attempted, with the definition of T^* maintained as given in Eq. (8). In the third temperature zone corresponding to $Ac_1 \leq T \leq Ac_3$, that is, the intercritical region, a third fit is attempted, with the definition of T^* given by following equation.

$$T^* = (T - Ac_p)/Ac_p. \qquad (9)$$

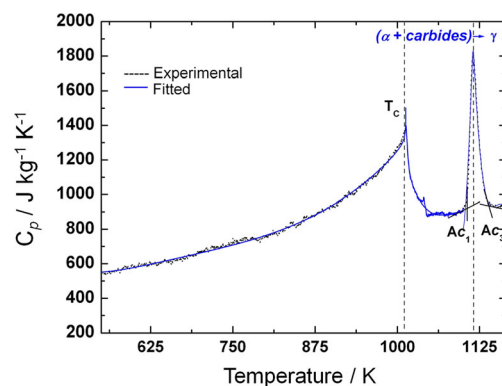The fit coefficients are listed in Table 6.

Fig. 6 Measured C_p variation with temperature for T91 steel base metal

Table 6 Listing of numerical values for the fit-coefficients in the expression for $C_P(T) = A + BT + CT^2 + DT^{-2} + E \exp(F\,T^*)(T^*)^G$

Sample	Temp. (K)	A (J kg^{-1} K^{-1})	B (J kg^{-1} K^{-2})	C (J kg^{-1} K^3)	D (J kg^{-1} K)	E (J kg^{-1} K)	F	G
Base metal	T < 1013	2.12×10^4	−33.55769	0.01621	-2.585812×10^9	7.4531	10.96518	−0.38618
	T < 1013	-1.64×10^6	2.01474×10^3	−0.69629	3.211966×10^{11}	9.23525×10^2	−4.73754	0.15369
	1100–1150	-4.67×10^7	5.44656×10^4	−17.83752	1.0169×10^{13}	7.50856×10^3	−16.09265	0.00335
WM-A	T > 1014	2.14514	−32.68614	0.01492	-2.972980×10^9	24.27478	9.52885	−0.19959
	T > 1014	2.103423×10^4	−33.04859	0.01477	-3.000657×10^9	7.56331×10^2	−7.99835	−0.04972
	1100–1150	-1.469058×10^4	1.72207×10^4	−5.67439	3.1626×10^{12}	1.3751×10^3	−59.27955	0.02756
WM-B	T < 1014	2.051805×10^4	−31.16466	0.01403	-2.840258×10^9	20.43526	9.63457	−0.29279
	T < 1014	2.022076×10^4	−31.35508	0.014	-3.168230×10^9	8.47936×10^2	−12.52792	−0.01597
	1100–1150	-2.147145×10^7	2.49193×10^4	−8.12826	4.706×10^{12}	7.17043×10^4	−6.92634	0.00046
WM-D	T > 1015	2.064892×10^4	−28.29548	0.01201	-3.588535×10^9	87.76339	7.90026	−0.1691
	T > 1015	2.965835×10^4	−23.90832	0.00432	-9.65624×10^9	3.35509×10^2	−40.54832	−0.09203
	1100–1150	-3.890724×10^7	4.55225×10^4	−14.96943	8.4061×10^{12}	-1.36456×10^5	−14.5786	1.0535

4.6 Bulk thermal expansion measurement

In Fig. 7, the measured temperature variation of $\Delta l_T/l_o = l_T - l_o/l_o$ is presented for the T91 base metal. The quantity l_o is taken as the starting length of the sample at T = 300 K. A heating rate of 5–7 K min^{-1} is selected for estimating bulk thermal expansion measurements. The Ac_1 and Ac_3 transformation temperatures recorded by dilatometry upon continuous heating are 1114 and 1140 ± 10 K, respectively. On the other hand, the $\gamma \rightarrow \alpha'$-martensite transformation is recorded in the temperature interval, $M_s = 634$ K, and $M_f = 559$ K. The Ac_1 and Ac_3 values as measured by dilatometry compare reasonably with the corresponding slow-scan dynamic calorimetry estimates of $Ac_1 = 1102$ K and $Ac_3 = 1138$ K (Table 3). As shown in Fig. 7, the transformation onset and finish temperatures are estimated by the method of intersection of leading tangents, and this procedure is known to introduce some error, especially when the transformation finish portion exhibits a long tail, as for example in Fig. 7, for α-ferrite + carbides $\rightarrow \gamma$-austenite phase change. Further, the Curie temperature T_c is not clearly seen in the dilatometry trace, owing to the
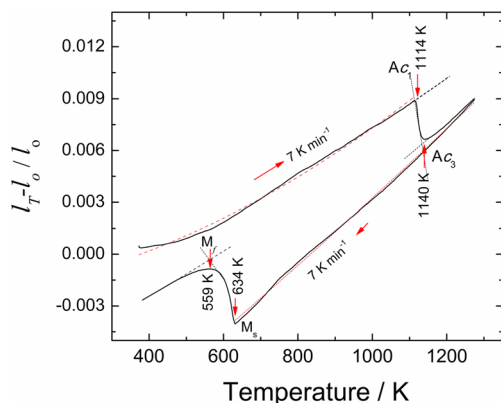

Fig. 7 Temperature variation of relative length change for T91 base metal

comparatively small magnitude of $\Delta l_T/l_o$ accompanying $\alpha_{ferro} \rightarrow \alpha_{para}$ transition. It is also evident from Fig. 7, that during cooling the metastable γ-austenite undergoes some phase change before undergoing displacive phase transition to α'-martensite at M_s, as delineated by the marked shift in the linear trend exhibited by $\Delta l_T/l_o$ with decreasing temperature. This aspect will however not be discussed in this study.

For the purpose of estimating bulk linear thermal expansion coefficient, the measured temperature dependency of $\Delta l_T/l_o$ has to be treated in a nontrivial manner [45]. Since, 9 % Cr-based steels are ferromagnetic in nature the presence of magnetism makes a small, but important contribution to lattice expansion [46]. Thus, to a first approximation, the total $\Delta l_T/l_o$ may be written as a sum of lattice and magnetic contributions [45, 46] as given below.

$$\Delta l_T/l_o = (\Delta l_T/l_o)_{lat} + (\Delta l_T/l_o)_{mag} \quad (10)$$

In Eq. (10), $(\Delta l_T/l_o)_{lat}$ represents the lattice contribution to the observed thermal strain, while $(\Delta l_T/l_o)_{mag}$ is the corresponding contribution arising from magnetic spins. Usually, $(\Delta l_T/l_o)_{lat}$ is the dominant contribution, while $(\Delta l_T/l_o)_{mag}$, which is often small and negative, assumes importance at low temperatures. In the present study, the measured $(\Delta l_T/l_o)$ is fitted to the following quadratic functional representation in the temperature range 473–1150 K.

$$(\Delta l_T/l_o) = -0.0022 + 3.634 \times 10^{-6}T + 5.873 \times 10^{-9}T^2 \quad (11)$$

It must be mentioned that the above fit smoothens the minor oscillations witnessed in 300–650 K region, which are thought to be associated with carbide dissolution reactions and also due to neglected magnetic contributions. It is hoped that this simplified representation is adequate for the purpose of obtaining engineering estimates of mean thermal expansion coefficients. The relative linear thermal expansion coefficient (α_l) in the

α-ferrite + carbide domain can now be obtained from Eq. (11) in the following manner.

$$\alpha_l = d(\Delta l_T/l_o)/dT = 3.634 \times 10^{-6} + 11.746 \times 10^{-9}T \quad (12)$$

The mean linear thermal expansion coefficient (α_m) with respect to T = 300 K on the other hand may be obtained from the relation,

$$\alpha_m = (\Delta l_T/l_o)/(T-300) \quad (13)$$

It is found that at T = 400 K, the estimated α_l for T91 steel takes the value of 0.78×10^{-5} K^{-1}, while at T = 1100 K, it is about 1.6×10^{-5} K^{-1}. In the same temperature interval, the mean linear thermal expansion coefficient α_m varies in the range, 0.19×10^{-5} to 1.12×10^{-5} K^{-1}.

5 Discussion

5.1 Transformation characteristics

In Fig. 8, the calculated carbon isolpleth or vertical section using Thermocalc sand TCFE6 steel database, for a typical T91 composition, with some W and Ta additions (ignoring S, P contents; for the sake of less complication), is shown. It may be seen that under ideal thermodynamic equilibrium conditions, the observed solidification path is a sensitive function of carbon content, which is an austenite stabilizer. It emerges from Fig. 8, that for a carbon content, which is slightly in excess of about 0.12 mass percent, there is a definite probability of obtaining L + γ + δ three phase coexistence even under equilibrium cooling. In case of F-M steels, having a higher

Ni + Mn content, this possibility is further enhanced. In this way, it is possible to rationalize the observed L + γ + δ three-phase coexistence during solidification sequence in the present slow-scan calorimetry experiments. However, while interpreting the solidification behavior observed under welding conditions (fast cooling), it is necessary to augment the simple thermodynamic picture with thermal history dictated kinetic simulations. This aspect is not included as a part of this study (Fig. 9).

One of the major outcomes of this investigation is the elucidation of the effect of (Ni + Mn) content on transformation temperatures. From the point of view of basic welding metallurgy of high chromium ferritic-martensitic steels, two basic considerations contribute to the proper choice of the welding consumable composition. They are as follows:

1. Nature of the solidification mode
2. On-heating Ac$_1$ temperature, an appropriate value of which decides the PWHT schedule

A standard manifestation of the thermodynamic balance between α-ferrite-and γ-austenite-stabilizing elements is the Ac$_1$ temperature. It must also be remembered that Ac$_1$ is influenced by kinetic factors as well. The knowledge of Ac$_3$ on the other hand is called for in rationalizing heat treatments like solutionizing, normalizing, or any other hot working process that is done in the fully austenitic phase field. These requirements are easily satisfied by going in for a slightly higher content of austenite-stabilizing elements in the overall weld metal composition. But then, an arbitrary enhancement of the stability of γ-austenite by the way of increasing, for example, the combined (Ni + Mn) content or adding Co, is however not recommended. This is because of the fact that this option interferes with the PWHT temperature and would also result in a concomitant lowering of M$_s$, the martensite start temperature. A low value for M$_s$ comes in the way of realizing a fully martensite microstructure in weld deposits [47]. This latter aspect gains importance in W and Ta containing high chromium steels [12, 13]. The presence of W and Ta is known to
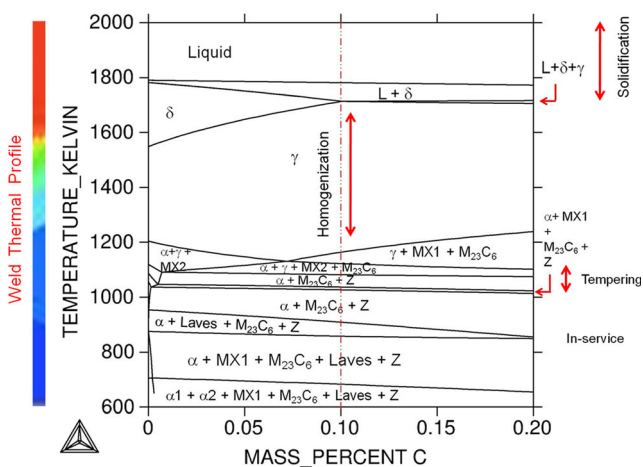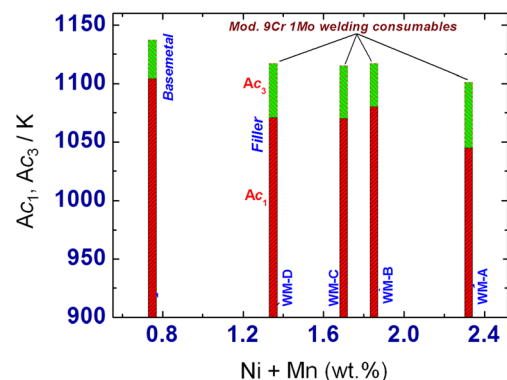

Fig. 8 ThermoCalc with TCFE6 database-based simulation of phase equilibria in a typical modified 9Cr-1Mo-Nb-V-Ta-W steel. Various phase fields as well as heat treatment domains are marked for easy identification. It is noteworthy that in a welding operation, the entire phase sequence indicated above is experienced over a very short time span, resulting in formation of nonequilibrium microstructure. The *pseudo-color bar on left* stands for the effect of decreasing temperature on phase equilibria

Fig. 9 Variation of Ac$_1$ and Ac$_3$ transformation temperatures with respect to combined (Ni + Mn) content

result in the formation of some δ-ferrite phase. In any case, the presence of a duplex microstructure having δ-ferrite islands is inimical to toughness and creep ductility [2].

The present results on Ac_1 can be satisfactorily fitted to the following modified empirical relation which was given originally by Santella et al. for 9 % Cr-1Mo steels [48].

$$(Ac_1/^oC) = 855 - 25.9(Ni + Mn/wt.\%) - 4.0(Ni + Mn/wt.\%)^2 \tag{14}$$

Unfortunately, the number of experimental data points catering to different (Ni + Mn) levels is rather limited to support a robust statistical analysis of present results, but nevertheless, the qualitative trend advocated by above empirical relation is in accord with the basic tenets of metallurgy. Further work on other compositions is currently underway.

5.2 α-Ferrite + carbides → γ-austenite transformation

The second objective of this study is concerned with the kinetics of α-ferrite + carbides → γ-austenite transformation on heating. Admittedly, the formation of austenite from tempered martensitic microstructure is not a simple metallurgical phenomenon [48–55]. It is clear that upon reaching Ac_1, the lower critical temperature, both the dissolution of carbide and the structural transformation of α-ferrite → γ-austenite are energetically feasible, yet, on account of kinetic factors, these concurrent reactions occur with different rates [28–30]. Of these, the structural transformation of (carbon-lean) α-ferrite to γ-austenite is basically an interface diffusion-controlled process [35, 49, 50, 53, 54], while carbide dissolution is a bulk- or volume-diffusion-controlled phenomenon [56, 57]. The heterogeneous nucleation of γ-austenite in α-ferrite is catalyzed by the presence of abundant internal interfaces to begin with, although at later stages, some other less potent nucleation sites need to get activated. Thus, in principle, the nucleation rate of austenite is one of continuously decreasing with time. However, assuming that nucleation of austenite is adequately facilitated the issue then is one of sustaining its growth by enabling the transfer of atoms across the growing austenite/ferrite interface [36]. From a mechanistic point of view, the austenite growth is possible even at high heating rates [52], if it is mediated by the transfer of mobile species across the growing γ/α interface.

In the case of carbide dissolution, however, the steep concentration gradient prevailing at the carbide/austenite or carbide/ferrite interfaces, both with respect to the slow diffusing substitutional elements (Cr, Mo) and also to some extent with respect to the relatively fast moving carbon atoms [56], dictates that volume diffusion is the rate-limiting step [27, 30]. With this conceptual background, the role of heating rate in influencing the kinetics of carbide dissolution and, hence, indirectly the austenitization reaction is discussed next.

For very slow heating rates, the system can be assumed to evolve with the possibility of realizing local thermodynamic equilibrium at the interface. Under such circumstances, it is likely that the carbide dissolution may get initiated even at relatively lower degree of superheating, that is $T > Ac_1$. The reaction proceeds to some extent, but certainly not to completion upon reaching Ac_3. The dissolution of carbides results in a gradual change in austenite composition in the immediate vicinity and this affects subsequent austenite formation kinetics in an indirect manner by affecting an increase in the activation energy for carbon diffusion in austenite.

If, on the contrary, the austenitization is sought under relatively fast heating conditions, the time scales provided are simply inadequate for the successful progress of carbide dissolution [25]. Nevertheless, the ferrite to austenite structural change can still be realized at these higher heating rates, with possibly a different mechanism, as the work of Kaluba et al. [52] has demonstrated. But, even in such a case, it is highly unlikely that transformation to austenite proceeds to 100 % completion upon reaching Ac_3. The presence of undissolved carbide particles may pin and retard the advancement of γ/α interface. A slight superheating and or isothermal hold above Ac_3 are required to realize the complete formation of homogeneous austenite [33]. For intermediate heating rates, the actual picture is rather intermediate in the sense that both carbide dissolution and α → γ phase change may proceed to different extents.

In terms of accounting for observed Q_{eff}, it may be said that Q_{eff} is reflective of the simple interface diffusion controlled α → γ structural change under fast heating conditions. However, for slower heating rates, it is influenced certainly by the disintegration of the carbide phase and its dissolution in the growing austenite phase. Judging the present results in the light of the picture portrayed above, the gradual decrease in Q_{eff} values with increasing β is thus rationalized. One final point is that the measured values of Q_{eff} is of the same order as that of the activation energy for chromium diffusion in the austenite phase of a low alloy–low carbon steel (~260 kJ mol^{-1}) [58]. However, the present estimate of Q_{eff} is in direct contradiction to the normal value of about 110–120 kJ mol^{-1} quoted for austenitization reaction in plain carbon or low-alloy steels, wherein the cementite or pearlite colony dissolution is more readily enabled as compared to $M_{23}C_6$ dissolution in high chromium steels. The higher values of Q_{eff} encountered in 9Cr-1Mo steels implies that simple carbon diffusion in austenite model is not applicable for the α → γ reaction in high-chromium steels used in power plants. The experimental study of Lenel [28, 29] and the electron microscopy characterization of austenite formation reaction in high-chromium model alloys by Shtansky et al [30] adequately reinforce this viewpoint. It must be added that in a recent study on the experimental measurement of α/γ interface mobility during austenite formation from ferrite in interstitial-free low-alloy

steels and in high pure iron, an effective activation energy of about 287 kJ mol^{-1} is reported for the interface-controlled transformation [53]. A review of available literature reveals that the understanding of the kinetics of austenite formation and carbide dissolution in high-chromium steels used in both thermal and nuclear power plants is still far from complete and more studies are needed to shed further light on this important issue.

5.3 Thermal properties

It must be mentioned that determination of thermal properties of various weld consumables has been undertaken as a part of data generation exercise toward facilitating engineering design and process simulation. In our general survey, we found that often times, reliable experimental data on heat capacity, bulk expansion, liquidus, solidus temperatures, and transformation enthalpies are not available for many newer varieties of advanced structural materials, and that some crude approximation has to be made from designer's point of view. It is in this light that we attempted to generate thermal property data on weld consumables. A preliminary survey revealed that data generated in this study are in expected trend for other similar 9 % Cr-based steels. However, what is pending is further experimentation on obtaining thermal diffusivity and elastic property data as a function of temperature, thus completing the full agenda of generating basic thermophysical data on high chromium F-M steels.

The results of this study toward understanding the transformation behavior of 9Cr-Mo-V-Nb-Ni-Mn containing weld consumables form an integral part of knowledge base development on improved versions of matching welding consumables, with improved service performance. Presently, there is a concerted worldwide effort toward developing advanced 9–12 % Cr ferritic-martensitic steels for increasing the operating temperature of power plants. There has been considerable success toward developing improved base materials. However, one of the impediments to their commercial appeal is the availability of appropriate welding consumables that can match the properties of improved base materials. Inputs from this work are expected to be useful in enabling a better understanding of basic issues and systematic design of improved welding consumables and also optimizing their heat treatment schedule.

6 Conclusions

1. A comprehensive differential scanning calorimetry characterization of thermal stability has been performed on four different varieties of modified 9Cr-1Mo welding consumables. Precise measurements of α-ferrite + carbide $\rightarrow$ γ-austenite transformation temperatures as a function of heating rate have also been made.

2. The transformation temperatures Ac_1 and Ac_3 are found to exhibit a strong nonlinear variation with heating rate, with the net effect of expanding the $\alpha + \gamma$ two-phase or intercritical region to higher temperatures for higher rates of heating.

3. It is found that for nominally the same Cr and Mo contents, the transformation temperatures Ac_1 and Ac_3 exhibit a decrease with respect to increasing (Ni + Mn) concentration. A high value of (Mn + Ni) content is also found to record a lower enthalpy for the α-ferrite + carbide $\rightarrow$ γ-austenite phase change.

4. The kinetics of the α-ferrite + carbide $\rightarrow$ γ-austenite transformation has been modeled after standard KJMA formalism, and the apparent activation energy for the overall phase change is estimated to be about 320-280 kJ mol^{-1}. The activation energy is found to be sensitive to the heating rate; it decreases for increasing heating rates.

5. For higher heating rates, it is suggested that the kinetics of α-ferrite + carbide $\rightarrow$ γ-austenite transformation is found to be mainly interface controlled as no significant carbide dissolution is realized under such circumstance. For slow heating, the accompanying $M_{23}C_6$ carbide dissolution in growing austenite also makes an indirect contribution to overall activation energy.

6. The variations of specific heat and bulk thermal expansion with temperature have been quantitatively estimated.

References

1. Sharafat S, Odette GR, Blanchard J (2009) J Nucl Mater 386–388: 896–899
2. Ellis FV, Henry JF, Roberts BW (1990) Welding, fabrication and service experience with modified 9Cr1Mo steel. In: New alloys for pressure vessels and piping, PVP volume 201. American Society for Mechanical Engineering, New York, pp 55–63
3. Masuyama F (2001) ISIJ Int 241:612–625
4. Klueh RL (2005) Int Mater Rev 50:287–310
5. Tamura M, Hayakawa H, Tamimura M, Hishunuma A (1988) Kondo T 155–157:620–625
6. Van der Schaff B, Gelles DS, Jitsukawa S, Kimura A, Klueh RL, Moslang AL, Odette GR (2000) J Nucl Mater 283–287:52–59
7. Ukai S, Harada M, Okada H, Inoue M, Nomura S, Shikakura S, Asabe K, Nishida T, Fujiwara M (1993) J Nucl Mater 204:65–73
8. Shirzadi A, Jackson S (2014) Structural alloys for power plants: operational challenges and high temperature materials. Woodhead Publ, Elsevier, London
9. Albert SK, Das CR, Bhaduri, AK (2002) In: Specifications for modified 9Cr-1Mo welding electrodes, IGCAR Internal report, PFBR, 33010 SP 1006.
10. Ehrlich K (2001) Fus Eng Des 56–57:71–82
11. Klueh RL, Nelson AT (2007) J Nucl Mater 371:37–52
12. Faulkner RG, Williams JA, Gonzalez-Sanchez E, Marshall AW (2003) Mater Sci Technol 19:347–354
13. Ravi K, Raju S, Mythili R, Saroja S, Jayakumar T, Rajendrakumar E (2015) Steel Res 86:1–16
14. Onoro J (2006) Int J Press Vessel Pip 83:540–545

15. Castro RJ, Cadenet JJ (1968) Welding metallurgy of stainless and heat resisting steels. Cambridge University Press, London
16. Pickering FB (1978) Physical metallurgy and the design of steels. Applied Science Publishers, London
17. AWS Welding Handbook (1998) Vol. 4: Materials and applications, 8th edition, Ohio, USA.
18. Sanderson SJ (1978) Interrelationship between mechanical properties and microstructure in a 9Cr-1Mo steel, In: ferritic steels for fast reactors, 1978th edn. BNES, London, p 120
19. Raju S, Arun Kumar NS, Jeyaganesh B, Mohandas E, Kamachi Mudali U (2007) J Alloys Compd 440:173–177
20. Raju S, Jeyaganesh B, Rai AK, Mythili R, Saroja S, Mohandas E, Vijayalakshmi M, Rao KBS (2009) Baldev Raj. J Nucl Mater 389: 385–393
21. Jeyaganesh B, Raju S, Rai AK, Mohandas E, Vijayalakshmi M, Rao KBS (2011) Baldev Raj. Mater Sci Technol 27:500–512
22. Desai PD (1986) J Phys Chem Ref Data 15:967–972
23. Raju S, Tripathy H, Rai AK, Hajra RN, Saroja S, Jayakumar T, Rajendrakumar R (2015) J Nucl Mater 459:150–158
24. Baltusnikas A, Levinskas R (2006) Mater Sci 12:192–198
25. Danon A, Servant C, Alamo A, Brachet JC (2003) Mater Sci Engg 348A:122–132
26. Schaffernak BC, Cerjak HH (2001) Calphad 25:241–251
27. Schneidner A, Inden G 92005) Acta Mater 53:519-526.
28. Lenel UR (1983) Scr Metall 47:471–474
29. Lenel UR, Honeycombe RWK (1984) Metal Sci 18:201–205
30. Shtansky DV, Nakai K, Ohmori Y (1999) Z Metallkd 90:25–37
31. Fu JW, Yang YS, Guo JJ, Tang WH (2008) Mater Sci Technol 24: 941–944
32. Hunter A, Ferry M (2002) Scr Mater 46:253–258
33. Raju S, Jeyagnaesh B, Banerjee A, Mohandas E (2007) Mater Sci Eng 465A:29–37
34. Liu FC, Sommer F, Mittemeijer EJ (2004) Acta Mater 52:2549–2560
35. Gamsjager E, Militzer M, Fazeli F, Svoboda J, Fischer FD (2006) Comp Mater Sci 37:94–100
36. Thiessen RG, Richardson IM, Sietsma J (2006) Mater Sci Eng 247A:225–231
37. Gaffard V, Gourgues-Lorenzon AF, Besson J (2005) ISIJ Int 45: 1015–1024
38. Starink MJ (2004) Int Mater Rev 49:191–226
39. Christian JW (1975) The theory of phase transformations in metals and alloys, part I, chapter 12, Pergamon, London.
40. Ruitenberg G, Woldt E, Petrford-Long AK (2001) Thermochim Acta 378:97–105
41. Vyazovkin S (2006) J Therm Anal Calorim 83:45–51
42. Liu F, Sommer F, Mittemeijer EJ (2004) J Mater Sci 39:1621–1634
43. Jeyaganesh B, Raju S, Mohandas M, Vijayalakshmi M (2008) Def Diff Forum 279:85–90
44. Kempen ATW, Sommer F, Mittemeijer EJ (2002) Thermochim Acta 383:21–30
45. Raju S, Tripathy H, Rai AK, Hajra RN, Saroja S, Jayakumar T, Rajendrakumar E (2015) J Nucl Mater 450:150–158
46. Pepperhoff W, Acet M (2001) Constitution and magnetism of iron and its alloys. Springer, Berlin
47. Onoro J (2006) J Mater Process Technol 180:137–142
48. Santella ML, Swindeman, RW, Reed RW, Tanzosh, JM (2001), In: Martensite formation in 9Cr-1Mo steel weld metal and its effect on creep behavior, ORNL Internal Report; http://www.ornl.gov/~webworks/cppr/y2001/pres/113751.pdf, pp. 1–6.
49. Hillert M, Nilsson K (1971) Torndahl. J Iron Steel Inst 209:49–66
50. Reed RC, Akbay T, Shen Z, Robinson JM, Root JH (1998) Mater Sci Engg A256:152–165
51. Zhang W, Elmer JW, Deb Roy T (2002) 26:753-757
52. Kaluba WJ, Taillard R, Foct J (1998) Acta Mater 46:5917–5925
53. Schmidt E, Soltesz D, Roberts S, Bednar A, Sridhar S (2006) ISIJ Int 46:1500–1509
54. Sietsma J, van der Zwagg S (2004) Acta Mater 52:4143–4152
55. Oliveira FLG, Andrade MS, Cota AB (2007) Mater Character 58: 256–261
56. Bjarbo A, Hatterstrand M (2001) Metall Mater Trans 32A:19–27
57. Hald J, Korcakova L (2003) ISIJ Int 43:420–427
58. Tokei Z, Hennessen K, Viefhaus H, Grabke HJ (2000) Mater Sci Technol 16:1129–1138